# Long-range dynamic polarization potentials for $^{11}$Li + $^{208}$Pb and $^{6}$He + $^{208}$Pb systems

W. Y. So
*Department of Radiological Science, Kangwon National University at Dogye, Samcheok 245-905, Korea*

K. S. Kim*
*School of Liberal Arts and Science, Korea Aerospace University, Koyang 412-791, Korea*

K. S. Choi and Myung-Ki Cheoun†
*Department of Physics, Soongsil University, Seoul 156-743, Korea*
(Received 1 September 2014; published 20 November 2014)

We investigate the effects of long-range dynamic polarization on elastic cross sections for heavy-ion collisions which comprise the Coulomb dipole excitation (CDE) potential and the long-range nuclear (LRN) potential. To study these effects, we perform a $\chi^2$ analysis for the elastic cross sections of $^{11}$Li + $^{208}$Pb and $^{6}$He + $^{208}$Pb systems using the long-range dynamic polarization potentials. For the CDE we formulate some empirical models to reproduce the experimental Coulomb dipole strength $B(E1)$ distribution and apply to the collision of $^{11}$Li and $^{6}$He. But the CDE potential turns out to be not enough to explain the experimental data relevant to the nuclei. It leads us to additionally take the LRN potential peculiar to these halo nuclei into account. Our model, which was constructed by adding the CDE and LRN potentials to the conventional short-range nuclear potential corrected by the Coulomb interaction, provides a good description of the experimental data. In particular, the surface type is shown to be more reasonable rather than the volume type in the LRN potential.

DOI: 10.1103/PhysRevC.90.054615 PACS number(s): 24.10.−i, 24.70.+s, 25.70.Jj

## I. INTRODUCTION

Borromean nuclei such as $^{6}$He, $^{11}$Li, and $^{14}$Be consist of a core nucleus and two valence neutrons, which are bound together, but all two-body systems (core nucleus–valence neutron or valence neutron–valence neutron) are unbound. This feature is well explained by one- and two-neutron separation energies for $^{6}$He, $^{11}$Li, and $^{14}$Be nuclei, as tabulated in Table I, where two-neutron separation energies are shown to be smaller than one-neutron separation energies. This implies that a system composed of a core nucleus and a valence neutron such as $^{5}$He, $^{10}$Li, and $^{13}$Be cannot be bound, while the addition of one more valance neutron to the system can make the system bound.

Another feature of Borromean nuclei is a halo structure arising from the two valence neutrons being far away from the core nucleus. Tanihata *et al.* [1,2] found that $^{11}$Li has a long tail in its matter distribution and Al-Khalili *et al.* [3] obtained the root-mean-square (rms) radii of He, Li, Be, and B isotopes using Glauber model calculations [4]. Since then, more detailed experiments and calculations have been reported. Sánchez *et al.* [5] measured the nuclear charge radii of Li isotopes by using the high-precision laser spectroscopy and compared the charge radius of $^{11}$Li with those of other Li isotopes through various methods. Esbensen *et al.* [6] measured the charge radius and the dipole response of $^{11}$Li from a three-body model and investigated the relevance of these measured values and the mean-square distance between the $^{9}$Li core nucleus and the center of mass of the two valence neutrons. All data recapitulated in Table II show that the matter radii of the Borromean nuclei are unexpectedly much larger than those of the core nuclei. This feature is confirmed to be caused by the matter density distribution of the weakly bounded valence neutron far away from the core nucleus. As a result, the matter radii of Borromean nuclei have a long tail (see Fig. 7 of Ref. [7]).

The other noteworthy feature for Borromean nuclei is the Coulomb dipole phenomena at low excitation energies [8–23]. Because the incident halo or weakly bound nuclei are composed of a core nucleus and valence neutrons, the charged core nuclei are decelerated by the Coulomb repulsive field generated from the target nuclei, but the valence neutrons are not affected by the Coulomb field. Consequently, the core nucleus and the valence neutrons in the incident halo or weakly bound nuclei are easily broken up compared to the tightly bound core nuclei, which have somewhat large valence-neutron separation energies. This phenomenon is called electric dipole polarization or Coulomb dipole excitation (CDE). It is well known that the breakup or direct reaction cross section is increased while the elastic cross section is decreased owing to the CDE. The reason for this is that the breakup or the direct reaction channels of the CDE are opened more easily than the elastic channel in heavy-ion collisions.

Andrés *et al.* [10–12] proposed an analytic complex polarization potential form without any adiabaticity correction factor $g_1(\xi)$ [24,25] with the usual adiabatic parameter $\xi$ as a function of the excitation energy for the CDE. They investigated the CDE effects coupled to breakup states for the $^{11}$Li + $^{208}$Pb system by using a dynamic complex polarization potential at $E_{\rm lab} = 24$ and 50 MeV. In this calculation, they used the Coulomb dipole strength $B(E1)$ distribution of Zinser *et al.* [23], which is fitted by a sum of two Gaussian functions,

*kyungsik@kau.ac.kr
†cheoun@ssu.ac.kr

 

TABLE I. One- and two-neutron separation energies for $^{6}$He, $^{11}$Li, and $^{14}$Be nuclei.

| Nucleus | $S_n$ (MeV) | $S_{2n}$ (MeV) |
|---|---|---|
| $^{6}$He | 1.71 | 0.98 |
| $^{11}$Li | 0.40 | 0.37 |
| $^{14}$Be | 1.78 | 1.27 |

and also used the two-neutron separation energies $S_{2n}$ for $^{11}$Li nuclei as 0.295 MeV. However, a new experimental result was reported on the Coulomb dipole strength distribution by Nakamura *et al.* [19], and the current two-neutron separation energy $S_{2n}$ for $^{11}$Li nuclei is known to be 0.37 MeV (Table I). It is an interesting point that the Coulomb dipole strength distribution of Ref. [19] compared with other experimental results [20–23] is considerably larger in the low-excitation-energy region (see Fig. 3 of Ref. [19]).

Kakuee *et al.* [8] investigated the CDE effect for the $^{6}$He + $^{208}$Pb system using the analytic complex polarization potential form proposed in Refs. [10–12]. They utilized a complex nuclear potential with a volume type of Woods-Saxon potential and obtained a large value of the imaginary diffuseness parameter from $\chi^2$ fitting. For the same system, Sánchez-Benítez *et al.* [9] also studied the CDE effect with the same method as in Ref. [8] and also obtained a large diffuseness parameter. They performed an additional calculation to study the energy dependence of the optical potential and the dispersion relation [26]. To investigate these features, they divided the complex nuclear potential into short- and long-range Woods-Saxon potentials. From this approach, they found that the CDE potential and the long-range nuclear (LRN) potential may account for the long-range absorption.

Recently, considering all of these things, we studied the CDE effects for the $^{11}$Li + $^{208}$Pb system [15]. In the calculation, however, we did not use the Coulomb dipole strength distribution in Ref. [19], but rather we used a dipole resonance energy $\varepsilon = 0.69$ MeV, which is extracted from the Coulomb dipole strength distribution of Ref. [19], to obtain the Coulomb dipole strengths $B(E1)$. As a result, the Coulomb dipole strengths are extracted as 1.42 and 1.41 $e^2$ fm$^2$ at $E_{\text{c.m.}} = 23.1$ and 28.3 MeV, respectively. These values are consistent with the experimental values obtained from Ref. [19]: $B(E1) = 1.42 \pm 0.18$ $e^2$ fm$^2$.

TABLE II. Root-mean-square matter radii for $^{4,6}$He, $^{9,11}$Li, and $^{12,14}$Be nuclei.

| Nucleus | rms matter radii (fm) | |
|---|---|---|
| | Reference [2] | Reference [3] |
| $^{4}$He | $1.57 \pm 0.04$ | $1.58 \pm 0.04$ |
| $^{6}$He | $2.48 \pm 0.03$ | $2.71 \pm 0.04$ |
| $^{9}$Li | $2.32 \pm 0.02$ | $2.30 \pm 0.02$ |
| $^{11}$Li | $3.12 \pm 0.16$ | $3.53 \pm 0.10$ |
| $^{12}$Be | $2.59 \pm 0.06$ | $2.54 \pm 0.05$ |
| $^{14}$Be | $3.16 \pm 0.38$ | $3.20 \pm 0.30$ |

The goal of the present work is to investigate the effect of long-range dynamic polarization potentials for elastic scattering of incident Borromean nuclei on heavy target nuclei using not only a short-range nuclear (SRN) potential corrected by the conventional Coulomb potential but also both a CDE potential [10–12] and a LRN potential [9,15] to take into account long-range interactions. In the present work, we also consider the new Coulomb dipole strength distribution [19] and the two-neutron separation energy $S_{2n} = 0.37$ MeV for $^{11}$Li nuclei. We also discuss the effect stemming from the difference between the volume type and surface type on the LRN potential. Finally, we extend this work to the $^{6}$He + $^{208}$Pb system. In Sec. II, we review briefly the experimental data. In Sec. III, we describe the $^{11}$Li + $^{208}$Pb system with adjusted potential parameters and obtain the Coulomb dipole strength $B(E1)$. We study the $^{6}$He + $^{208}$Pb system in Sec. IV. Finally, we summarize the present work in Sec. V.

## II. REVIEW OF EXPERIMENTAL DATA

In this section we discuss the ratio of the elastic scattering cross sections to the Rutherford cross section $P_E$, given by

$$P_E \equiv \frac{d\sigma_{el}}{d\Omega} \Big/ \frac{d\sigma_C}{d\Omega} = \frac{d\sigma_{el}}{d\sigma_C}, \tag{1}$$

where $d\sigma_{el}/d\Omega$ and $d\sigma_C/d\Omega$ represent the elastic and Coulomb scattering cross sections, respectively [27,28]. In Fig. 1, we plot the experimental ratio for (a) $^{4}$He + $^{208}$Pb and $^{6}$He + $^{208}$Pb systems and (b) $^{9}$Li + $^{208}$Pb and $^{11}$Li + $^{208}$Pb systems. The ratio is presented as a function of the reduced distance $d$, by which the closest distance is given by $D = d(A_1^{1/3} + A_2^{1/3})$. Figure 1(a) shows data for $^{4}$He + $^{208}$Pb and $^{6}$He + $^{208}$Pb systems at $E_{\text{lab}} = 22$ MeV, and Fig. 1(b) shows data for $^{9}$Li + $^{208}$Pb and $^{11}$Li + $^{208}$Pb systems at $E_{\text{c.m.}} = 28.3$ MeV, which is the center-of-mass energy. Here $A_1$ and $A_2$ are the masses of the projectile and the target nuclei. Because the SRN force has no effect in the far-distance region, the Coulomb force influences only the projectile, so that the ratio $P_E$ approaches unity. In the close-distance region, in which sufficient nuclear force becomes of importance, however, the value of $P_E$ starts to fall off around the interaction distance $d_I$, as shown in Fig. 1.

In general, the interaction distances $d_I$ for tightly bound nuclei such as $^{12}$C and $^{16}$O are about 1.6 fm [29], but those of weakly bound nuclei such as $^{6}$He, $^{6,7,8}$Li, and $^{9}$Be are much larger [30,31]. In Ref. [31], we have already obtained the interaction distances of $^{6,7,8}$Li, which lie between 1.8 and 2.1 fm. By using the same method as in Ref. [31], the interaction distances $d_I$ for $^{9}$Li and $^{11}$Li become $\sim$1.9 and $\sim$5.5 fm, respectively. Because $^{9}$Li is a relatively tightly bound nucleus, the interaction distance is close to that of other nuclei such as $^{6,7,8}$Li and $^{9}$Be. However, the interaction distances of $^{6}$He and $^{11}$Li are very long because they are very loosely bound nuclei owing to the two valence neutrons. This means that the breakup process easily takes place at forward angles or in the far-distance region, as shown in Fig. 1. It is well known that this behavior of $^{6}$He and $^{11}$Li was related to the CDE potential effect [10–12] and the LRN potential effect [8,9].

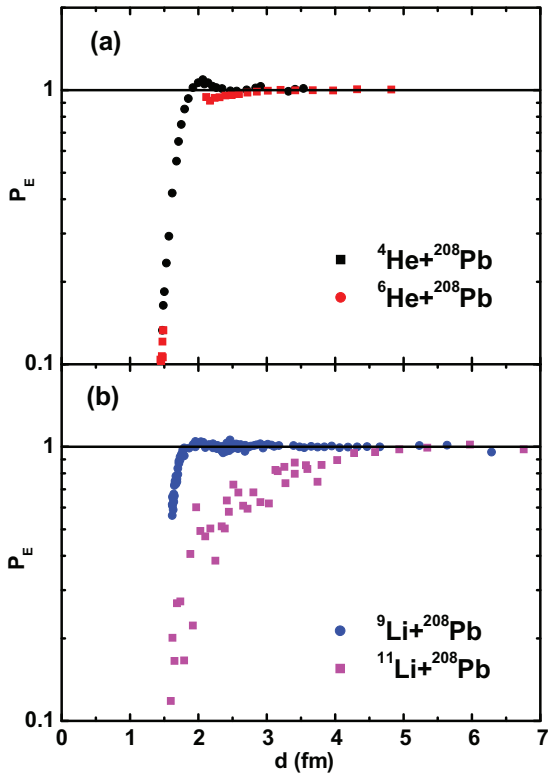


FIG. 1. (Color online) Ratios of the elastic scattering cross sections to the Rutherford cross section $P_E$, as a function of the reduced distance $d$ at (a) $E_{\rm lab} = 22$ MeV for $^4$He + $^{208}$Pb and $^6$He + $^{208}$Pb systems and (b) $E_{\rm c.m.} = 28.3$ MeV for $^9$Li + $^{208}$Pb and $^{11}$Li + $^{208}$Pb systems. The data are taken from Ref. [9] for $^4$He + $^{208}$Pb and $^6$He + $^{208}$Pb systems and from Ref. [13] for $^9$Li + $^{208}$Pb and $^{11}$Li + $^{208}$Pb systems.

## III. OPTICAL MODEL CALCULATIONS

First, we consider the $^{11}$Li + $^{208}$Pb system. To explain the breakup effect for the $^{11}$Li + $^{208}$Pb system, we use the following optical model Scrödinger equation:

$$[E - T_l(r)]\chi_l^{(+)}(r) = U_{\rm OM}(r)\chi_l^{(+)}(r), \tag{2}$$

where $\chi_l^{(+)}(r)$ is the partial decomposed distorted wave function. The kinetic energy operator $T_l(r)$ is given by

$$T_l(r) = -\frac{\hbar^2}{2\mu}\left(\frac{d^2}{dr^2} - \frac{l(l+1)}{r^2}\right), \tag{3}$$

where $\mu$ and $l$ are the reduced mass and the angular momentum, respectively. The optical model potential $U_{\rm OM}(r)$ is generally given by

$$U_{\rm OM}(r) = U_C(r) - [V_0(r) + iW_0(r)], \tag{4}$$

where $U_C(r)$ denotes the Coulomb potential. $V_0(r)$ and $W_0(r)$ are the real and imaginary parts, respectively, of the optical model potential of the Woods-Saxon volume type given by [32]

$$V_0(r) + iW_0(r) = V_0(E)f(X_0) + iW_0(E)f(X_W), \tag{5}$$

where $f(X_i) = [1 + \exp(X_i)]^{-1}$ with $X_i = (r - R_i)/a_i$ ($i = 0$ and $W$) being the usual Woods-Saxon function, while $V_0(E)$ and $W_0(E)$ are the energy-dependent strength parameters of the real and imaginary parts, respectively.

TABLE III. Optical model parameters in the SRN potential for the $^9$Li + $^{208}$Pb system. Here, $r_i = R_i/(A_1^{1/3} + A_2^{1/3})$ with $i = 0$ and $W$.

| $V_0^{sh}$ (MeV) | $W_0^{sh}$ (MeV) | $a_0^{sh} = a_W^{sh}$ (fm) | $r_0^{sh} = r_W^{sh}$ (fm) |
|---|---|---|---|
| 56.50 | 26.60 | 0.82 | 1.10 |

### A. Short-range (or bare) nuclear potential

Because $^{11}$Li is composed of the core nucleus $^9$Li and two valence neutrons, we first extract the bare potential for $^{11}$Li + $^{208}$Pb from the optical model calculation. To extract the bare potential, using the elastic scattering data for the $^9$Li + $^{208}$Pb system, we obtain the optical model potential:

$$U_{\rm OM}^{^9{\rm Li}}(r) = U_C(r) - \left[V_0^{sh}(r) + iW_0^{sh}(r)\right], \tag{6}$$

where $V_0^{sh}(r)$ and $W_0^{sh}(r)$ are the real and imaginary parts, respectively, of the optical model potential. With the optical model potential, we already performed a $\chi^2$ analysis in Ref. [15] and obtained the best-fit parameters listed in Table III. For this calculation, we used the four parameters ($a_0^{sh}$, $a_W^{sh}$, $r_0^{sh}$, and $r_W^{sh}$) fixed in our previous calculations [15] and varied only two parameters ($V_0^{sh}$ and $W_0^{sh}$). Using these parameters we calculated the ratios $P_E$ and compared our results (solid lines) with the experimental data, as shown in Fig. 2. The red circles denote the experimental data taken from Ref. [13]. Our calculations describe the experimental data very well. Therefore the parameters in Table III can be used as the bare potential of the $^{11}$Li + $^{208}$Pb system. Note that the superscript "$sh$" in Eq. (6) means the SRN potential compared relatively to the LRN one, which will be described later.

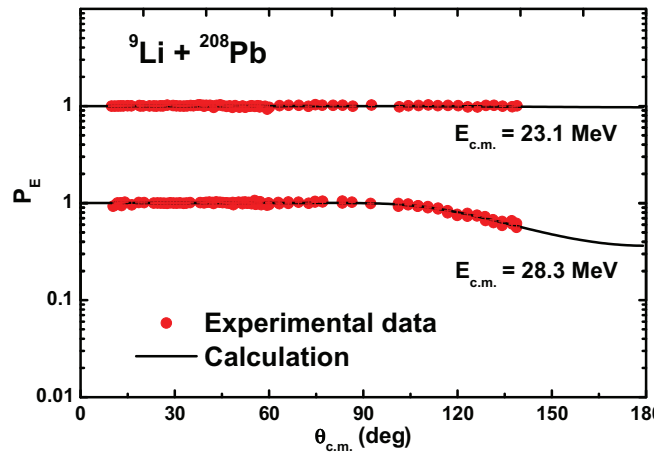


FIG. 2. (Color online) Ratios $P_E$ calculated with the SRN potential for $^9$Li + $^{208}$Pb. The solid line denotes the calculated ratios $P_E$ obtained by using Eq. (6) and the parameters in Table III. Red circles represent the experimental data taken from Ref. [13].

### B. Coulomb dipole excitation potential

To explain the strong absorption in the long-range region (or in the forward-angle region), which is peculiar to the Coulomb breakup reaction of halo systems [13], we need to consider a long-range potential. The CDE potential is known as the most significant long-range potential. To take into account the long-range interaction effect, we add a CDE potential [10–12] to Eq. (4) as follows:

$$U_{\rm OM}^{^{11}{\rm Li}}(r) = U_{\rm OM}^{^{9}{\rm Li}}(r) - U_{\rm CDE}(r) = U_C(r) - \left[V_0^{sh}(r) + iW_0^{sh}(r)\right] - U_{\rm CDE}(r), \quad (7)$$

where the additional CDE potential is written as

$$U_{\rm CDE}(r) = \frac{4\pi}{9}\frac{Z_2^2e^2}{\hbar v}\frac{1}{(r-a_0)^2 r}\int_{\varepsilon_b}^{\infty} d\varepsilon \frac{dB(E1)}{d\varepsilon} \times \left[g\left(\frac{r}{a_0}-1,\xi\right) + if\left(\frac{r}{a_0}-1,\xi\right)\right], \quad (8)$$

with

$$f\left(\frac{r}{a_0}-1,\xi\right) = 4\xi^2\left(\frac{r}{a_0}-1\right)^2 \times \exp(-\pi\xi)K''_{2i\xi}\left[2\xi\left(\frac{r}{a_0}-1\right)\right], \quad (9)$$

where $a_0 = Z_1Z_2e^2/2E_{\rm c.m.}$ is the distance of closest approach in head-on collisions, $Z_1$ and $Z_2$ denote charge numbers of the projectile and target nuclei, respectively, $K''$ is the second derivative of a modified Bessel function, and $\xi = a_0\varepsilon/\hbar v$ is the usual adiabatic parameter [12]. Here the real part of the CDE potential, $g(\frac{r}{a_0}-1,\xi)$, has to satisfy the dispersion relation with an imaginary part [10–12] as follows:

$$g\left(\frac{r}{a_0}-1,\xi\right) = \frac{P}{\pi}\int_{-\infty}^{\infty}\frac{f\left(\frac{r}{a_0}-1,\xi\right)}{\xi-\xi'}d\xi'. \quad (10)$$

In Eq. (8), $dB(E1)/d\varepsilon$ is the Coulomb dipole strength $B(E1)$ distribution along with the excitation energy $\varepsilon$. A number of studies for measuring this distribution have been performed [19–23]. In this work, the most recently measured $B(E1)$ distribution [19] is used.

We use some empirical models to reproduce the experimental Coulomb dipole strength $B(E1)$ distribution [19]. The first model, denoted as model 1 (M1), is given by

$$\left.\frac{dB(E1)}{d\varepsilon}\right|_{\rm M1} = N_1\frac{(\varepsilon-\varepsilon_b)}{(\varepsilon-\varepsilon_b-\Gamma_1/2)^2+(\Gamma_1/2)^2}. \quad (11)$$

This model is obtained by modifying the Breit-Wigner function in Ref. [20]. Note that $\varepsilon_b = 0.37$ MeV is equal to the two-neutron separation energy $S_{2n}$ for $^{11}$Li nuclei. $N_1$ and $\Gamma_1$ are the normalization constant and the width of the modified Breit-Wigner function, respectively. The second model, denoted as model 2 (M2) in Ref. [12], is written as

$$\left.\frac{dB(E1)}{d\varepsilon}\right|_{\rm M2} = N_1\frac{(\varepsilon-\varepsilon_b)^3}{\varepsilon^4}(1+t)^2\exp(-2t), \quad (12)$$

with $t = \frac{\varepsilon-\varepsilon_b}{\Gamma_1}$. As remarked in Ref. [12], this model is obtained from a simple analytic three-body calculation. As shown in Fig. 3, however, M2 does not satisfy the $B(E1)$ distribution in the high-excitation-energy region for $\varepsilon \gtrsim 1.1$ MeV. To satisfy the $B(E1)$ distribution there, we add a Gaussian-type function to Eq. (12). This is model 3 (M3) as follows:

$$\left.\frac{dB(E1)}{d\varepsilon}\right|_{\rm M3} = N_1\frac{(\varepsilon-\varepsilon_b)^3}{\varepsilon^4}(1+t)^2\exp(-2t) + \frac{N_2}{\varepsilon}\exp(-s^2), \quad (13)$$

with $t = \frac{\varepsilon-\varepsilon_b}{\Gamma_1}$ and $s = \frac{\varepsilon-\varepsilon_2}{\Gamma_2}$. $N_2$, $\varepsilon_2$, and $\Gamma_2$ are the normalization constant, the centroid, and the full width at half maximum of the additional Gaussian-type function, respectively. The parameters of each model and the integrated values of the Coulomb dipole strength distribution are listed in Table IV.

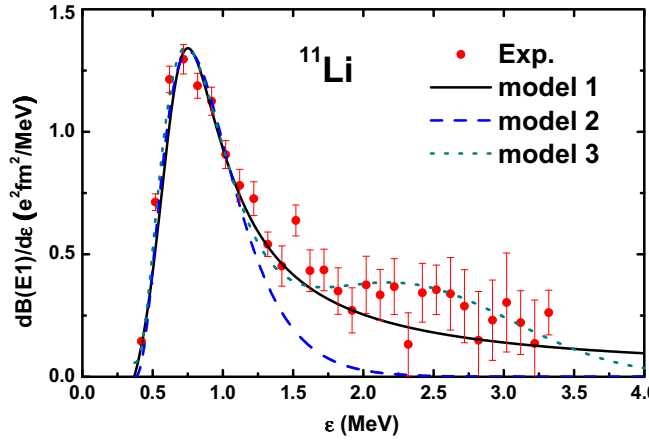


FIG. 3. (Color online) $B(E1)$ distributions for $^{11}$Li obtained from three models compared with the experimental data (red circles) taken from Ref. [19]. Solid (black), dashed (blue), and dotted (green) lines represent the $B(E1)$ distributions obtained from M1, M2, and M3, respectively.

The experimental Coulomb dipole strength value $B(E1)$ is obtained as $B(E1) = 1.42 \pm 0.18\ e^2\,{\rm fm}^2$ by measuring up to $\varepsilon = 3.37$ MeV in Ref. [19], and theoretical calculations obtained from the new s23 model [6] and the correlated single-particle model [33] are 1.38 and 1.57 $e^2\,{\rm fm}^2$, respectively. As shown in Table IV, these values are consistent with our results obtained from M1 and M3.

Figure 4 shows the ratios $P_E$ for the $^{11}{\rm Li} + ^{208}{\rm Pb}$ system calculated by using Eq. (7) with three $B(E1)$ distribution models for the pure dipole excitation. Our results do not

TABLE IV. Parameters of the Coulomb dipole strength $B(E1)$ distribution for each model. $B(E1)$ is the integrated value of the Coulomb dipole strength distribution up to excitation energy $\varepsilon = 3.0$ MeV for three models of $^{11}$Li nuclei.

| | $N_1$ | $\varepsilon_b$ (MeV) | $\Gamma_1$ (MeV) | $N_2$ | $\varepsilon_2$ (MeV) | $\Gamma_2$ (MeV) | $B(E1)$ ($e^2$ fm$^2$) |
|---|---|---|---|---|---|---|---|
| Model 1 (M1) | 0.30 | 0.37 | 0.54 | | | | 1.27 |
| Model 2 (M2) | 13.40 | 0.37 | 0.40 | | | | 0.88 |
| Model 3 (M3) | 14.00 | 0.37 | 0.36 | 0.90 | 2.50 | 1.10 | 1.49 |

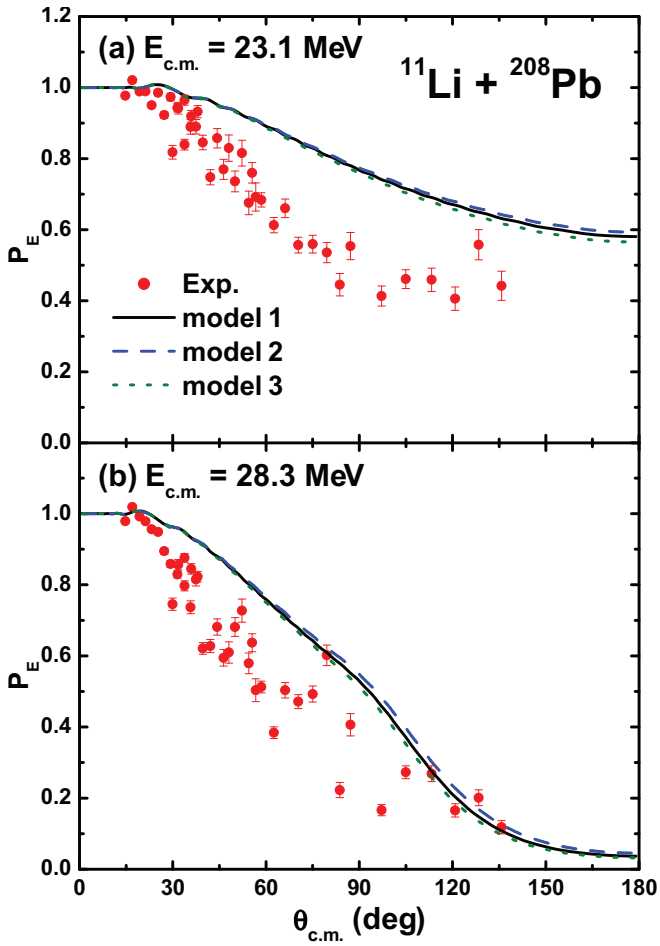


FIG. 4. (Color online) Ratios of the elastic scattering cross sections to the Rutherford cross section $P_E$, as a function of the scattering angle $\theta_{\rm c.m.}$ at $E_{\rm c.m.} = 23.1$ and 28.3 MeV for the $^{11}$Li + $^{208}$Pb system. Solid (black), dashed (blue), and dotted (green) lines are the calculated ratios $P_E$ obtained by using M1, M2, and M3, respectively, for the $^{11}$Li + $^{208}$Pb system. Red circles represent the experimental data for $^{11}$Li + $^{208}$Pb taken from Ref. [13]. Note that we only consider the SRN potential and the CDE potential in Eq. (7).

show any remarkable change for the models of the $B(E1)$ distribution. This means that the contribution of the $B(E1)$ distribution is not noticeable at $\varepsilon \geqslant 1.1$ MeV. When the excitation energy $\varepsilon$ (or the adiabaticity parameter $\xi$) decreases, both real and imaginary parts of the CDE potential $U_{\rm CDE}$ rapidly decrease owing to the exponential function in $f(\frac{r}{a_0} - 1, \xi)$ of Eq. (8). As shown in Fig. 3, the Coulomb dipole strength distribution of M2 does not match the experimental data at $\varepsilon \geqslant 1.1$ MeV, but the $B(E1)$ distribution of M3, which includes six parameters, quite accurately reproduces the experimental data of the Coulomb dipole strength distribution. Although M3 describes the experimental data well, it is very complicated. In the present work, therefore, we choose the simplest form M1 among the three $B(E1)$ distribution models.

If the breakup effect in the long-range region were only affected by the pure dipole excitation, we could have explained the ratio of the elastic scattering cross section data to the Rutherford cross section $P_E$ in Fig. 3 of Ref. [13]. However, our results are quite different from the experimental data. This implies that the breakup effect in the long-range region cannot be explained by only the pure CDE interaction, as shown in Fig. 4.

TABLE V. Geometrical parameters of the LRN potential with (a) the volume type and (b) the surface type of Woods-Saxon potential used in Eq. (14) for the $^{11}$Li + $^{208}$Pb system.

| Type | $E_{\rm c.m.}$ (MeV) | $V_0^{lo}$ (MeV) | $W_0^{lo}$ (MeV) | $a_0^{lo} = a_W^{lo}$ (fm) | $r_0^{lo} = r_W^{lo}$ (fm) | $\chi^2$ |
|---|---|---|---|---|---|---|
| (a) Volume | 23.1 | − 34.40 | 3.83 | 4.00 | 1.10 | 9.4 |
| | 28.3 | − 23.40 | 3.09 | 4.00 | 1.10 | 14.5 |
| (b) Surface | 23.1 | − 9.10 | 0.99 | 3.42 | 1.44 | 10.0 |
| | 28.3 | − 6.01 | 0.75 | 3.42 | 1.44 | 14.3 |

### C. Long-range nuclear potential

As done in Refs. [9,15], we add another LRN as follows: The optical model potential $U_{\rm OM}^{^{11}{\rm Li}}(r)$ including the additional LRN complex polarization potential $U_{\rm OM}^{lo}$ is written as

$$\begin{aligned} U_{\rm OM}^{^{11}{\rm Li}}(r) &= U_{\rm OM}^{^{9}{\rm Li}}(r) - U_{\rm CDE}(r) - U_{\rm OM}^{lo}(r) \\ &= U_C(r) - \left[V_0^{sh}(r) + i W_0^{sh}(r)\right] \\ &\quad - U_{\rm CDE}(r) - \left[V_0^{lo}(r) + i W_0^{lo}(r)\right]. \end{aligned} \tag{14}$$

References [9,15] exploit the volume-type Woods-Saxon form with large diffuseness parameters $a_0^{lo}$ and $a_W^{lo}$ in the additional LRN potential. In the present work, we fix radii $r_0^{lo} = r_W^{lo} = 1.10$ fm and diffuseness parameters $a_0^{lo} = a_W^{lo} = 4.00$ fm as done in Table III of Ref. [15]. To obtain potential depth parameters $V_0^{lo}$ and $W_0^{lo}$, we perform a $\chi^2$ analysis with fixed radii and diffuseness values. The best-fit potential depth parameters $V_0^{lo}$ and $W_0^{lo}$ are listed in rows (a) of Table V. Note that potential depths of the real part in the LRN potential $V_0^{lo}$ have negative values. The negative potential depth plays an important role of increasing the Coulomb barrier energy and reducing the absorption cross section. Using these parameters, we obtained the ratios $P_E$ [solid (black) line] in Fig. 5.

Until now, for the effect of LRN potentials in the collision of incident Borromean nuclei and heavy target nuclei, we have made use of the CDE potential and the two nuclear potentials (SRN and LRN) with a volume-type Woods-Saxon potential. For the two volume-type Woods-Saxon potentials, the inner region of the SRN and the LRN potential overlaps because they have the same radius. However, the breakup reaction mainly occurs at the surface region of the Borromean nuclei because the two valence neutrons are away from the core nuclei. Therefore, for the LRN potential in Eq. (14), the surface-type Woods-Saxon potential is conjectured to be more reasonable to explain the breakup reaction.

To obtain geometric parameters of the surface-type Woods-Saxon potential, we first perform a $\chi^2$ analysis by using four adjustable parameters, which are $V_0^{lo}$, $W_0^{lo}$, $a_0^{lo} = a_W^{lo}$, and $r_0^{lo} = r_W^{lo}$, for all incident energies and then fix the radius parameter as the average value of radii obtained from the fitting. As a result,

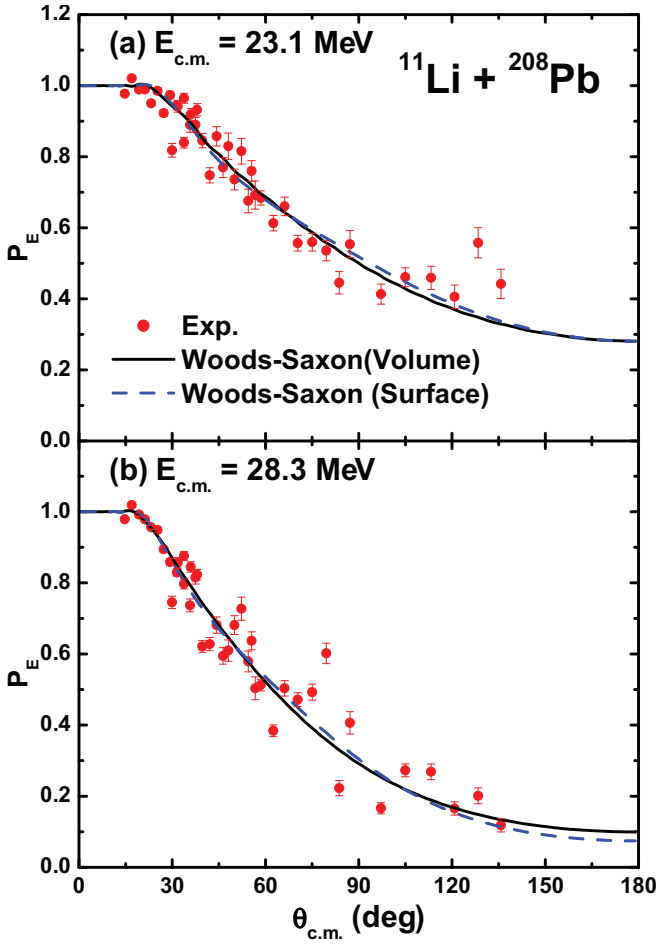


FIG. 5. (Color online) Same as in Fig. 4, but including the additional LRN potential in Eq. (14). Note that we only consider M1.

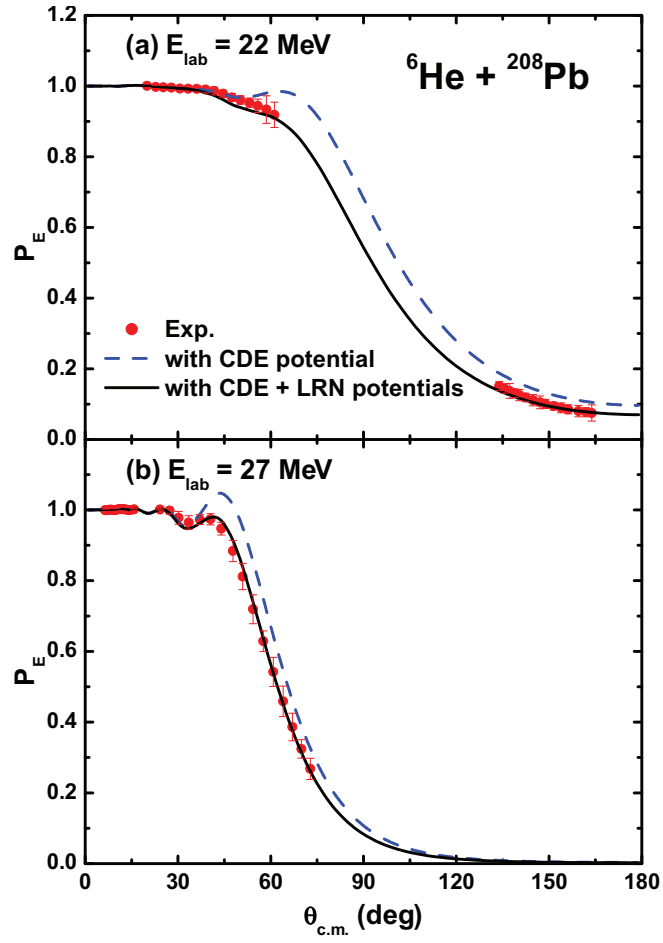


FIG. 6. (Color online) Same as Fig. 4, but for the $^{6}$He + $^{208}$Pb system. The solid (black) line is for the SRN potential and two long-range dynamic polarization potentials including the CDE and LRN potentials; the dashed (blue) line is for only the SRN potential and the CDE potential obtained by using M1. Red circles represent the experimental data for $^{6}$He + $^{208}$Pb taken from Refs. [8,9].

we get the radius of the surface-type Woods-Saxon potential, which is about $r_0^{lo} = r_W^{lo} = 1.44$ fm, and then we repeat the $\chi^2$ analysis for three adjustable parameters ($V_0^{lo}$, $W_0^{lo}$, and $a_0^{lo} = a_W^{lo}$) at a fixed radius. From this analysis, we obtain diffuseness parameters $a_0^{lo} = a_W^{lo} = 3.42$ fm as the average value. After fixing the radius and the diffuseness parameters, finally, we perform a $\chi^2$ analysis for two adjustable parameters ($V_0^{lo}$ and $W_0^{lo}$). The best-fit potential depth parameters $V_0^{lo}$ and $W_0^{lo}$ are listed in rows (b) of Table V and the ratios $P_E$ [dashed (blue) line] are plotted in Fig. 5. We find that the two methods provide almost the same results except for the radius and the diffuseness of LRN potentials. For the case of the volume-type Woods-Saxon potential, its radius is short compared with that of the surface-type one, but it is found that the reduction of the radius can be offset by the enhancement of the diffuseness.

## IV. APPLICATION TO THE $^{6}$He + $^{208}$Pb SYSTEM

As done in the $^{11}$Li + $^{208}$Pb system, we first find parameters of the SRN potential for the $^{6}$He + $^{208}$Pb system by performing a $\chi^2$ analysis with the elastic scattering data for the $^{4}$He + $^{208}$Pb system [34]. Note that we fix the radius and the diffuseness ($a_0^{sh} = a_W^{sh} = 0.82$ fm and $r_0^{sh} = r_W^{sh} = 1.10$ fm) as parameters used in the $^{11}$Li + $^{208}$Pb system. As a result, the best potential depths of the real and imaginary potentials obtained from the $\chi^2$ analysis are extracted as $V_0^{sh} = 44.62$ MeV and $W_0^{sh} = 28.07$ MeV, respectively. The dashed (blue) line in Fig. 6 shows the ratios $P_E$ for the pure CDE using the SRN potential set ($V_0^{sh}$, $W_0^{sh}$, $a_0^{sh} = a_W^{sh}$, and $r_0^{sh} = r_W^{sh}$) with the $B(E1)$ distribution from the M1 model in Fig. 7. The parameters of the $B(E1)$ distribution for the $^{6}$He nucleus are listed in Table VI. There are two theoretical calculations for the $B(E1)$ distributions in Refs. [16,17]. However, the calculated $B(E1)$ distributions overall do not satisfy the experimental data in

TABLE VI. Same as in Table IV, but for $^{6}$He nuclei using M1.

| | $N_1$ | $\varepsilon_b$ (MeV) | $\Gamma_1$ (MeV) | $N_2$ | $\varepsilon_2$ (MeV) | $\Gamma_2$ (MeV) | $B(E1)$ ($e^2$ fm$^2$) |
|---|---|---|---|---|---|---|---|
| Model 1 (M1) | 0.26 | 0.98 | 2.70 | | | | 0.71 |

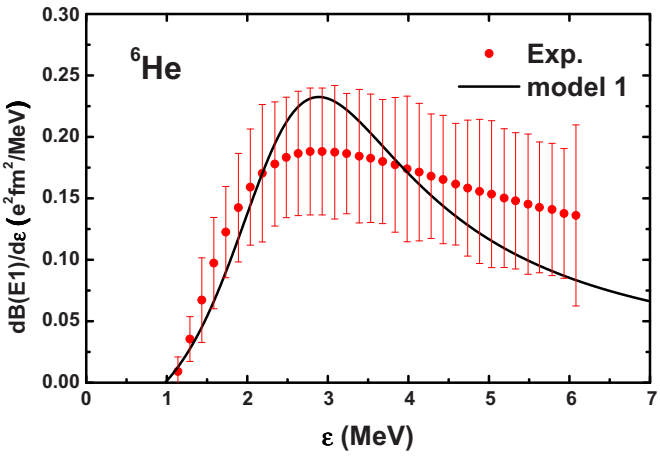


FIG. 7. (Color online) Same as Fig. 3, but for the $B(E1)$ distribution of $^6$He nuclei obtained from M1. Red circles represent the experimental data for $^6\mathrm{He} + ^{208}\mathrm{Pb}$ taken from Ref. [18].

the low-excitation-energy region (see Fig. 4 of Ref. [18]). As shown in Fig. 7, our M1 result satisfies the experimental data within the error, especially in the low-energy region, but the shape is different from that of the experimental data. Although our $B(E1)$ curve has a different shape, the value of $B(E1)$ using M1 is 0.71 $e^2$ fm$^2$, which agrees with the other theoretical value (0.71 $e^2$fm$^2$ [17]) and with the experimental data (0.59 $\pm$ 0.12 $e^2$ fm$^2$ [18]).

As shown in Fig. 6, our results (dashed lines) from the SRN potential and the pure CDE potential using the $B(E1)$ distribution with M1 overestimate the experimental data. To resolve the discrepancy, we have to add the LRN potential with a surface-type Woods-Saxon potential similarly to the case of $^{11}$Li.

First, we extract the geometric parameters of the surface-type Woods-Saxon potential by using a $\chi^2$ analysis as done in the $^{11}\mathrm{Li} + ^{208}\mathrm{Pb}$ system. The geometric parameters obtained from the $\chi^2$ analysis are listed in Table VII, and the dispersion relations of the real and the imaginary parts for the LRN potential are shown in Fig. 8. The values of the strength parameters of the LRN potential extracted by using the $\chi^2$ analysis, $V_0^{lo}(E)$ and $W_0^{lo}(E)$, are denoted by the red and the black solid circles, respectively. Here we show also interpolated functions, $V_0^{lo}(E)$ and $W_0^{lo}(E)$, of the incident energy $E(=E_{\mathrm{lab}})$ extracted by the circle points. The imaginary strength parameter function $W_0^{lo}(E)$ is summarized by the

TABLE VII. Same as in Table V, but for the $^6\mathrm{He} + ^{208}\mathrm{Pb}$ system using the surface type of Woods-Saxon potential.

| $E_{\mathrm{lab}}$ (MeV) | $V_0^{lo}$ (MeV) | $W_0^{lo}$ (MeV) | $a_0^{lo} = a_W^{lo}$ (fm) | $r_0^{lo} = r_W^{lo}$ (fm) | $\chi^2$ |
|---|---|---|---|---|---|
| 14 | 0.10 | 0.00 | 2.29 | 1.43 | 0.7 |
| 16 | 0.20 | 0.04 | 2.29 | 1.43 | 0.4 |
| 18 | 0.12 | 0.13 | 2.29 | 1.43 | 0.8 |
| 22 | 0.09 | 0.10 | 2.29 | 1.43 | 0.6 |
| 27 | $-$0.03 | 0.14 | 2.29 | 1.43 | 1.9 |

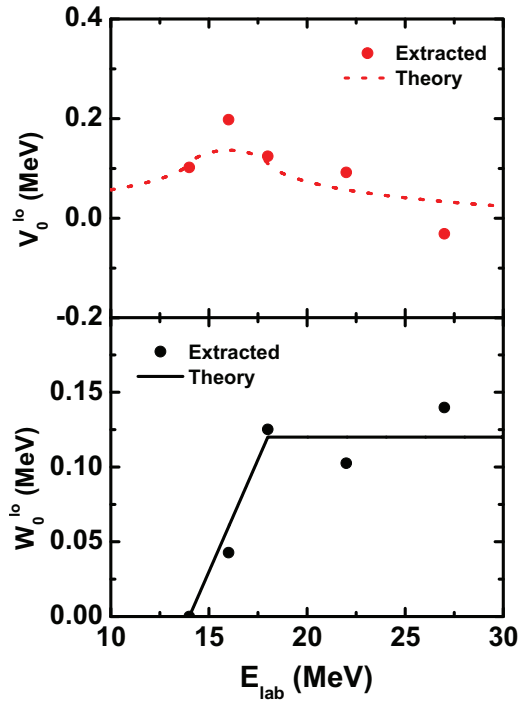


FIG. 8. (Color online) Real and imaginary strength functions, $V_0^{lo}(E)$ and $W_0^{lo}(E)$, as a function of the laboratory energy $E_{\mathrm{lab}}$. The solid (black) line in the lower panel denotes $W_0^{lo}(E)$ from Eq. (15) and the dotted (red) line in the upper panel represents $W_0^{lo}(E)$ obtained by using the dispersion relation.

following function of $E(=E_{\mathrm{lab}})$ (in units of MeV):

$$W_0^{lo}(E) = \begin{cases} 0 & \text{for } E = 14.0, \\ 0.03(E - 14.0) & \text{for } 14.0 < E \leqslant 18.0, \\ 0.12 & \text{for } 18.0 < E, \end{cases} \quad (15)$$

which is shown as the solid (black) line in the lower panel of Fig. 8. The dotted (red) line in the upper panel denotes $V_0^{lo}(E)$ obtained by the interpolation of the (red) points from the dispersion relation. Note that the dispersion relation obtained from this work is quite similar to that of Sánchez-Benítez *et al.* [9] except for the highest excitation energy $E_{\mathrm{lab}} =$ 27 MeV. According to Ref. [9], the extracted $W_0^{lo}(E)$ values gradually decrease at $E_{\mathrm{lab}} \geqslant 18$ MeV but $W_0^{lo}(E)$ values extracted from the present work are essentially constant. We chose three intervals to obtain $W_0^{lo}(E)$, but $W_0^{lo}(E)$ in Ref. [9] was obtained from four intervals, so that our results are a bit different from theirs. However, the interpolated $W_0^{lo}(E)$ function in Fig. 8 seems to have a constant value. Thus, even if we take our model, it is still premature to conclude that there exists a decrease of $W_0^{lo}(E)$ at higher excitation energies, as mentioned in Ref. [9].

Finally, we calculate the elastic cross sections and present the results in comparison with the experimental data in Figs. 6 and 9 using $W_0^{lo}(E)$ given by Eq. (15) and $V_0^{lo}(E)$ obtained by using the dispersion relation. The solid (black) line in Fig. 6 shows the ratios $P_E$ including the LRN potential, the CDE, and

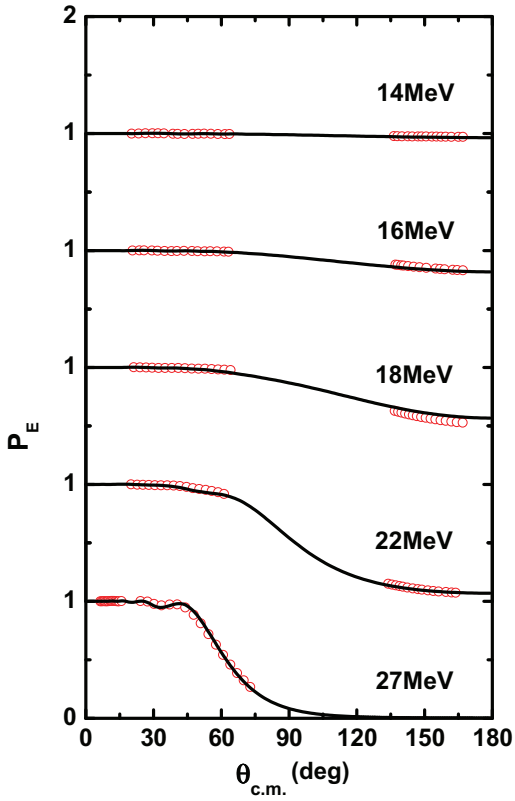


FIG. 9. (Color online) Same as Fig. 6, but with all incident laboratory energies considered.

the SRN potential set ($V_0^{sh}$, $W_0^{sh}$, $a_0^{sh} = a_W^{sh}$, and $r_0^{sh} = r_W^{sh}$). From Fig. 6, we find that both the CDE potential and the LRN potential have to be considered to explain the breakup reaction (or the direct reaction) process for heavy-ion collisions by Borromean nuclei. Figure 9 shows the ratios $P_E$ for all incident energies; these are also well matched to the experimental data.

## V. SUMMARY AND CONCLUSION

We investigated CDE and LRN potential effects on elastic cross sections in low-energy heavy-ion collisions by Borromean nuclei, $^{11}$Li and $^{6}$He. To take these effects into account, we exploited the optical model analysis, in which we included both a conventional SRN potential corrected by the Coulomb potential and a Coulomb dynamic polarization potential extracted by using the Coulomb dipole strength $B(E1)$ distributions. However, we found that these two potentials are not enough to explain the relevant experimental data. For a better understanding of the $P_E = d\sigma_{el}/d\sigma_C$ data, we introduced a LRN potential in addition to the two potentials. Using this dynamic imaginary polarization potential, we performed a $\chi^2$ analysis for the elastic cross section data obtained from heavy-ion collisions. From this analysis, we learned that the LRN potential as well as the CDE potential play a significant role in explaining the experimental data, specifically the strong absorption in the long-range region, for the heavy-ion collisions.

One more point to be noticed is that a surface-type potential in the LRN potential turns out to be more reasonable rather than a volume-type potential. We also found that the contribution of the $B(E1)$ distribution is not as significant in the high-excitation-energy region. As a result, the simplest form among the three $B(E1)$ distribution models (M1) could be used safely in our present work.

In conclusion, our dynamic polarization potentials furnish a good description of the experimental data and both the CDE potential and the LRN potential are needed to explain the breakup reaction.

## ACKNOWLEDGMENTS

The authors wish to express sincere thanks to Professor B. T. Kim for kindly reading the manuscript and providing useful comments. This work was supported by the National Research Foundation of Korea (Grants No. 2012R1A1A2041974, No. 2012M7A1A2055605, and No. 2014R1A2A2A05003548).

[1] I. Tanihata, H. Hamagaki, O. Hashimoto, Y. Shida, N. Yoshikawa, K. Sugimoto, O. Yamakawa, T. Kobayashi, and N. Takahashi, Phys. Rev. Lett. **55**, 2676 (1985).
[2] I. Tanihata, T. Kobayashi, O. Yamakawa, S. Shimoura, K. Ekuni, K. Sugimoto, N. Takahashi, T. Shimoda, and H. Sato, Phys. Lett. B **206**, 592 (1988).
[3] J. S. Al-Khalili, J. A. Tostevin, and I. J. Thompson, Phys. Rev. C **54**, 1843 (1996).
[4] R. J. Glauber, in *Lectures in Theoretical Physics*, edited by W. E. Brittin (Interscience, New York, 1959), Vol. 1, p. 315.
[5] R. Sánchez, W. Nörtershäuser, G. Ewald, D. Albers, J. Behr, P. Bricault, B. A. Bushaw, A. Dax, J. Dilling, M. Dombsky, G. W. F. Drake, S. Götte, R. Kirchner, H.-J. Kluge, Th. Kühl, J. Lassen, C. D. P. Levy, M. R. Pearson, E. J. Prime, V. Ryjkov, A. Wojtaszek, Z.-C. Yan, and C. Zimmermann, Phys. Rev. Lett. **96**, 033002 (2006).
[6] H. Esbensen, K. Hagino, P. Mueller, and H. Sagawa, Phys. Rev. C **76**, 024302 (2007).
[7] N. B. Shulgina, B. Jonson, and M. V. Zhukov, Nucl. Phys. A **825**, 175 (2009).
[8] O. R. Kakuee, J. Rahighi, A. M. Sánchez-Benítez, M. V. Andrés, S. Cherubini, T. Davinson, W. Galster, J. Gómez-Camacho, A. M. Laird, M. Lamehi-Rachti, I. Martel, A. C. Shotter, W. B. Smith, J. Vervier, and P. J. Woods, Nucl. Phys. A **728**, 339 (2003).
[9] A. M. Sánchez-Benítez, D. Escrig, M. A. G. Álvarez, M. V. Andrés, C. Angulo, M. J. G. Borge, J. Cabrera, S. Cherubini, P. Demaret, J. M. Espino, P. Figuera, M. Freer, J. E. García-Ramos, J. Gómez-Camacho, M. Gulino, O. R. Kakuee, I. Martel, C. Metelko, A. M. Moro, F. Pérez-Bernal, J. Rahighi, K. Rusek, D. Smirnov, O. Tengblad, P. Van Duppen, and V. Ziman, Nucl. Phys. A **803**, 30 (2008).
[10] M. V. Andrés, J. Gómez-Camacho, and M. A. Nagarajan, Nucl. Phys. A **579**, 273 (1994).
[11] M. V. Andrés, J. Gómez-Camacho, and M. A. Nagarajan, Nucl. Phys. A **583**, 817 (1995).

[12] M. V. Andrés and J. Gómez-Camacho, Phys. Rev. Lett. **82**, 1387 (1999).
[13] M. Cubero, J. P. Fernández-García, M. Rodríguez-Gallardo, L. Acosta, M. Alcorta, M. A. G. Alvarez, M. J. G. Borge, L. Buchmann, C. A. Diget, H. A. Falou, B. R. Fulton, H. O. U. Fynbo, D. Galaviz, J. Gómez-Camacho, R. Kanungo, J. A. Lay, M. Madurga, I. Martel, A. M. Moro, I. Mukha, T. Nilsson, A. M. Sánchez-Benítez, A. Shotter, O. Tengblad, and P. Walden, Phys. Rev. Lett. **109**, 262701 (2012).
[14] J. P. Fernández-García, M. Cubero, M. Rodríguez-Gallardo, L. Acosta, M. Alcorta, M. A. G. Alvarez, M. J. G. Borge, L. Buchmann, C. A. Diget, H. A. Falou, B. R. Fulton, H. O. U. Fynbo, D. Galaviz, J. Gómez-Camacho, R. Kanungo, J. A. Lay, M. Madurga, I. Martel, A. M. Moro, I. Mukha, T. Nilsson, A. M. Sánchez-Benítez, A. Shotter, O. Tengblad, and P. Walden, Phys. Rev. Lett. **110**, 142701 (2013).
[15] W. Y. So, K. S. Kim, and Myung-Ki Cheoun, Phys. Rev. C **89**, 057601 (2014).
[16] A. Cobis, D. V. Fedorov, and A. S. Jensen, Phys. Rev. Lett. **79**, 2411 (1997).
[17] B. V. Danilin, I. J. Thompson, J. S. Vaagen, and M. V. Zhukov, Nucl. Phys. A **632**, 383 (1998).
[18] T. Aumann, D. Aleksandrov, L. Axelsson, T. Baumann, M. J. G. Borge, L. V. Chulkov, J. Cub, W. Dostal, B. Eberlein, Th. W. Elze, H. Emling, H. Geissel, V. Z. Goldberg, M. Golovkov, A. Grünschloß, M. Hellström, K. Hencken, J. Holeczek, R. Holzmann, B. Jonson, A. A. Korshenninikov, J. V. Kratz, G. Kraus, R. Kulessa, Y. Leifels, A. Leistenschneider, T. Leth, I. Mukha, G. Münzenberg, F. Nickel, T. Nilsson, G. Nyman, B. Petersen, M. Pfützner, A. Richter, K. Riisager, C. Scheidenberger, G. Schrieder, W. Schwab, H. Simon, M. H. Smedberg, M. Steiner, J. Stroth, A. Surowiec, T. Suzuki, O. Tengblad, and M. V. Zhukov, Phys. Rev. C **59**, 1252 (1999).
[19] T. Nakamura, A. M. Vinodkumar, T. Sugimoto, N. Aoi, H. Baba, D. Bazin, N. Fukuda, T. Gomi, H. Hasegawa, N. Imai, M. Ishihara, T. Kobayashi, Y. Kondo, T. Kubo, M. Miura, T. Motobayashi, H. Otsu, A. Saito, H. Sakurai, S. Shimoura, K. Watanabe, Y. X. Watanabe, T. Yakushiji, Y. Yanagisawa, and K. Yoneda, Phys. Rev. Lett. **96**, 252502 (2006).
[20] D. Sackett, K. Ieki, A. Galonsky, C. A. Bertulani, H. Esbensen, J. J. Kruse, W. G. Lynch, D. J. Morrissey, N. A. Orr, B. M. Sherrill, H. Schulz, A. Sustich, J. A. Winger, F. Deák, A. Horváth, Á. Kiss, Z. Seres, J. J. Kolata, R. E. Warner, and D. L. Humphrey, Phys. Rev. C **48**, 118 (1993).
[21] K. Ieki, D. Sackett, A. Galonsky, C. A. Bertulani, J. J. Kruse, W. G. Lynch, D. J. Morrissey, N. A. Orr, H. Schulz, B. M. Sherrill, A. Sustich, J. A. Winger, F. Deák, A. Horváth, Á. Kiss, Z. Seres, J. J. Kolata, R. E. Warner, and D. L. Humphrey, Phys. Rev. Lett. **70**, 730 (1993).
[22] S. Shimoura, T. Nakamura, M. Ishihara, N. Inabe, T. Kobayashi, T. Kubo, R. H. Siemssen, I. Tanihata, and Y. Watanabe, Phys. Lett. B **348**, 29 (1995).
[23] M. Zinser, E. Humbert, T. Nilsson, W. Schwab, H. Simon, T. Aumann, M. J. G. Borge, L. V. Chulkov, J. Cub, Th. W. Elze, H. Emling, H. Geissel, D. Guillemaud-Mueller, PG. Hansen, R. Holzmann, H. Imich, B. Jonson, J. V. Kratz, R. Kulessa, Y. Leifels, H. Lenske, A. Magel, A. C. Mueller, G. Münzenberg, F. Nickel, G. Nyman, A. Richter, K. Riisager, C. Scheidenberger, G. Schrieder, K. Stelzer, J. Stroth, A. Surowiec, O. Tengblad, E. Wajda, and E. Zude, Nucl. Phys. A **619**, 151 (1997).
[24] W. G. Love, T. Terasawa, and G. R. Satchler, Nucl. Phys. A **291**, 183 (1977).
[25] K. Alder, A. Bohr, T. Huus, B. Mottelson, and A. Winther, Rev. Mod. Phys. **28**, 432 (1956).
[26] C. C. Mahaux, H. Ngo, and G. R. Satchler, Nucl. Phys. A **449**, 354 (1986).
[27] W. Y. So, T. Udagawa, K. S. Kim, S. W. Hong, and B. T. Kim, Phys. Rev. C **75**, 024610 (2007).
[28] W. Y. So, T. Udagawa, K. S. Kim, S. W. Hong, and B. T. Kim, Phys. Rev. C **76**, 024613 (2007).
[29] G. R. Satchler, *Introduction to Nuclear Reactions* (Wiley, New York, 1980).
[30] W. Y. So, S. W. Hong, B. T. Kim, and T. Udagawa, Phys. Rev. C **69**, 064606 (2004).
[31] Woonyoung So, Taehyung Kim, Manseok Han, Hyungug Cho, Byeongyeon Moon, Sungjoong Kim, and Kyungsik Kim, J. Phys. Soc. Jpn. **82**, 044201 (2013).
[32] G. R. Satchler, *Direct Nucler Reactions* (Clarendon, Oxford, 1983).
[33] H. Esbensen and G. F. Bertsch, Nucl. Phys. A **542**, 310 (1992).
[34] A. R. Barnett and J. S. Lilley, Phys. Rev. C **9**, 2010 (1974).